ELSEVIER

Biophysical Chemistry 108 (2004) 165–185

Biophysical Chemistry

www.elsevier.com/locate/bpc

Fluorescence detection for the XLI analytical ultracentrifuge

Ian K. MacGregor, Arthur L. Anderson, Thomas M. Laue*

Center to Advance Molecular Interaction Science, University of New Hampshire, Durham, NH 03824, USA

Abstract

Analytical ultracentrifugation (AUC) provides first-principle hydrodynamic and thermodynamic information concerning the size, shape and interactions of macromolecules. The fundamental measurement needed in AUC is the macromolecular concentration as a function of radial position and time. Currently, the Beckman Coulter XLI analytical ultracentrifuge may be equipped with absorbance and refractive detectors, which provide complementary concentration determinations. For detecting trace quantities of materials, fluorescence detection offers unique advantages over either absorbance or interference detection. A prototype fluorescence detector for the XLI analytical ultracentrifuge has been developed and its characteristics determined. An Ar^+ laser provides a continuous 488-nm excitation beam. Radial resolution is achieved by scanning the focused beam along a radial axis. Detection of the fluorescence signal uses a co-axial, front-face optical configuration to reduce inaccuracies in the concentration caused by inner filter effects. A high-speed A/D data acquisition system allows the fluorescence intensity to be monitored continuously and at a sufficiently high angular resolution so that at any radial position the intensities from all of the samples may be acquired at each revolution. The fluorescence detector is capable of detecting concentrations as low as 300 pM for fluorescein-like labels. The radial resolution of the fluorescence detector is comparable to that of the absorbance system. Both sedimentation velocity and sedimentation equilibrium measurements may be made with the fluorescence detector. Results are presented comparing data acquired using the fluorescence with those acquired using the absorbance detector.

Keywords: Fluorescence detection; Analytical ultracentrifuge; Sedimentation equilibrium; Sedimentation velocity; Novel instrumentation

1. Introduction

Analytical ultracentrifugation (AUC) is a classical method of biochemistry and molecular biology. Because AUC relies on the principle property of mass and the fundamental laws of gravitation, it has broad applicability. The principle measurement in any AUC experiment is the concentration as a function of radial position and time. The Beckman Coulter XLI analytical ultracentrifuge comes equipped with absorbance and interference optics. Fluorescence detection can provide distinct advantages in sensitivity and selectivity over absorbance or interference optics, and would be a useful addition to the analytical ultracentrifuge.

Abbreviations: AUC, analytical ultracentrifugation; PMT, photomultiplier tube; GFP, green fluorescent protein; Ar^+, argon ion

*Corresponding author. CAMIS, University of New Hampshire, Room 379 Rudman Hall, 46 College Road, Durham, NH 03824-3544, USA. Tel.: +1-603-862-2459; fax: +1-603-862-0031.

E-mail address: tom.laue@unh.edu (T.M. Laue).

0301-4622/04/$ - see front matter © 2003 Elsevier B.V. All rights reserved.
doi:10.1016/j.bpc.2003.10.018

Riesner and colleagues have described a fluorescence detection system for the Beckman Model E analytical ultracentrifuge [1]. This detection system has excellent sensitivity and radial resolution. However, since the Model E has been replaced by the XLI, a new fluorescence detector is needed.

Presented here is the design and characterization of a fluorescence detector for the XLI. The new device is similar to the previous fluorescence detector in that it achieves a high radial resolution by moving the excitation beam, as a tiny spot of light, along a radial axis. However, the design of the new fluorescence detector is otherwise quite different in that it uses a co-axial, front-face layout to reduce inner-filter effects. Results from the new detector are compared to those from the absorbance system and show that the new fluorescence optics is useful for both equilibrium and velocity sedimentation experiments.

2. Design

2.1. Optics

The fluorescent optics uses a co-axial excitation and emission design similar to some confocal fluorescent microscopes (Fig. 1). Light originates from a continuous 50-mW Ar^+ laser tuned to 488 nm (Omnichrome Inc. 532-AP-OAR-AAM), and is coupled (Oz Optical HPUC-23-488-S-3.5AR-LH) into a 3.5-μm glass, single-mode fiber (Oz Optical SMJ-33-488-3.5/125-3-5-SP) that delivers the light to the remaining optics. The optical fiber passes into the centrifuge vacuum chamber through a custom-built feedthrough mounted in a manifold that also holds a 19-wire (22 gauge) electrical feedthrough and the XLI vacuum gauge. The manifold is threaded to replace the vacuum gauge, and 3/8-inch hole was drilled through the stainless-steel chamber liner and the aluminum temperature shroud to accommodate the optical fiber and the electrical wiring needed by the fluorescence optics.

Most of the optical system was constructed using components from the Spindler and Hoyer (now Linos Optical AG, Göttingen, Germany) 'Microbench' series (Fig. 1). For the excitation optical path, light spreads into a cone from the fiber optic tip (Fig. 1(1)) positioned at the focal point of a lens (Fig. 2(1)) to provide a collimated beam of light that is first directed using a silver elliptical mirror (Fig. 1(6)) attached to an adjustable mirror holder (Fig. 1(5)), then redirected toward the cell by a dichroic beam splitter attached to an adjustable mirror holder (Fig. 1(12 and 13)). The collimated excitation beam is brought to focus in the sample by a condensing lens (Fig. 1(8)), which also serves as the objective lens for the emission optical path.

The fluorescing sample will emit light in all directions at longer wavelengths than the excitation beam. Any emitted light passing through the focal point and captured by the objective lens (Fig. 1(8)) will be collimated and passed through the dichroic beam splitter. The dichroic beam splitter (Fig. 1(12)) reflects 95% of the light at wavelength shorter than 490 nm, which largely removes stray light at the excitation wavelength. The collimated emitted light is refocused (Fig. 1(14)) and passed through second long-pass filter (better than 95% transmittance at wavelengths >505 nm) (Fig. 1(15)). A spatial filter (Fig. 1(16)) is positioned at the focal point of the last lens before impinging on the photomultiplier tube (PMT) (Fig. 1(20)). A custom adapter attaches the PMT to a Spindler & Hoyer lens holder.

The entire optics stage (Fig. 2) is mounted on a vacuum-compatible stepping motor-driver stage (Oriel Inc. 16139). The stage position is controlled by the computer using a stepping motor controller (Oriel Inc. 20025). The optical assembly and stepping motor attach to two mounting posts mounted to the steel base plate of the vacuum chamber. The posts are designed to allow the entire optic assembly to be removed and replaced in the chamber without losing positional accuracy.

2.2. Electronics and signal processing

Current from the PMT is converted to voltage using a transconductance amplifier ($G=50\,000$ V/A), buffered using an LM 310 voltage follower, and digitized with 12-bit resolution (Computer Board Inc. CIO-DAS-16/M1, connected to a Computer Board MegaFifo data storage module with 8 MB of memory) for storage in a PC. Data acqui-

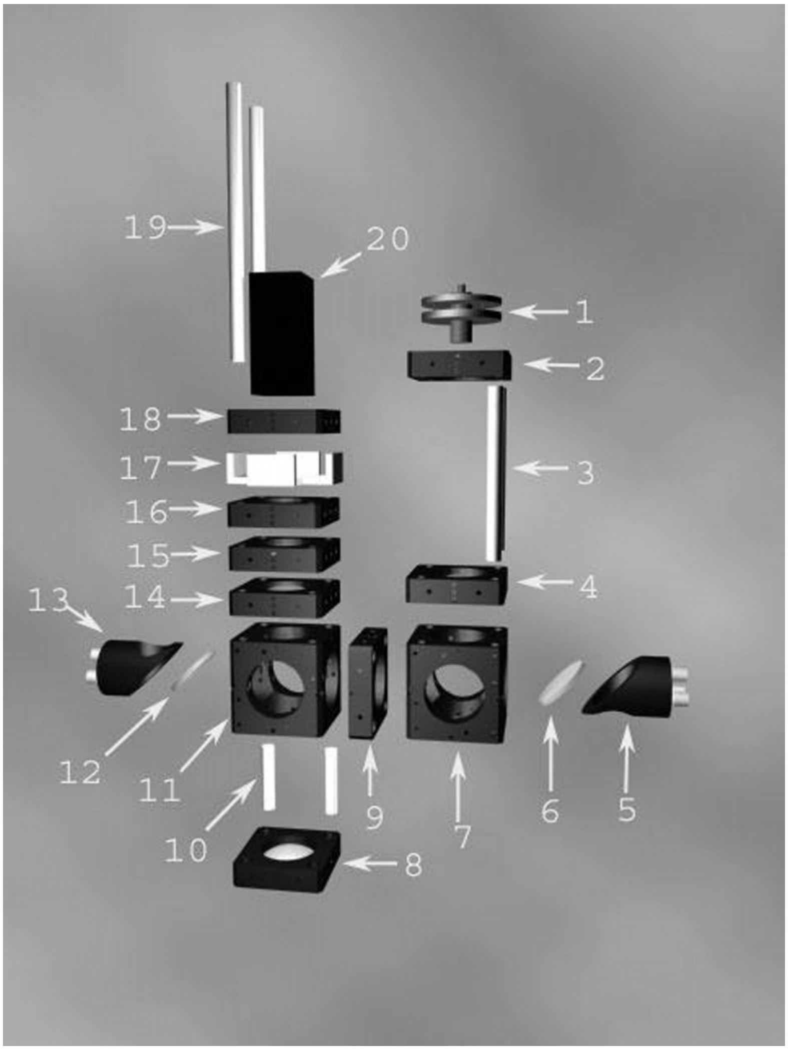

Fig. 1. Schematic of the unassembled confocal fluorescence optics. Specific items include: (1) fiber optic coupling (Oz Optical SPH-01 & HUCO-13); (2) mounting plate (Spindler & Hoyer 06-1010); (3) steel rod, 75 mm (Spindler & Hoyer 06-1209), (4) mounting plate (Spindler & Hoyer 06-1010) holding a 50-mm focal length acromatic lens (Spindler & Hoyer 06-3125); (5) beam steering mirror holder (Spindler & Hoyer 06-5086); (6) silver elliptical plane mirror (Spindler & Hoyer 34-0523); (7) mounting cube (Spindler & Hoyer 06-1080); (8) mounting plate (Spindler & Hoyer 06-1010) holding a 50-mm focal length acromatic lens (Spindler & Hoyer 06-3125); (9) mounting plate (Spindler & Hoyer 06-1042); (10) steel rod, 30 mm (Spindler & Hoyer 06-1208); (11) mounting cube (Spindler & Hoyer 06-1080); (12) dichroic beam splitter 488/514 nm (Spindler & Hoyer BSP-25-488514); (13) beam steering mirror holder (Spindler & Hoyer 06-5086); (14) mounting plate (Spindler & Hoyer 06-1010) holding a 40-mm focal length acromatic lens (Spindler & Hoyer 06-3127); (15) mounting plate (Spindler & Hoyer 06-1010), retaining rings (2) (Spindler & Hoyer 06-5069), long wave pass filter 495 nm cutoff (Spindler & Hoyer LWP-25-490); (16) mounting plate (Spindler & Hoyer 06-1010) holding a 0.6 mm diameter pinhole filter (Spindler & Hoyer 04-0177); (17) PMT adapter to Spindler & Hoyer mounting plate, custom made; (18) mounting plate (Spindler & Hoyer 06-1010); (19) steel rod, 150 mm (Spindler & Hoyer 06-1210); (20) PMT (Hamamatsu H5783).

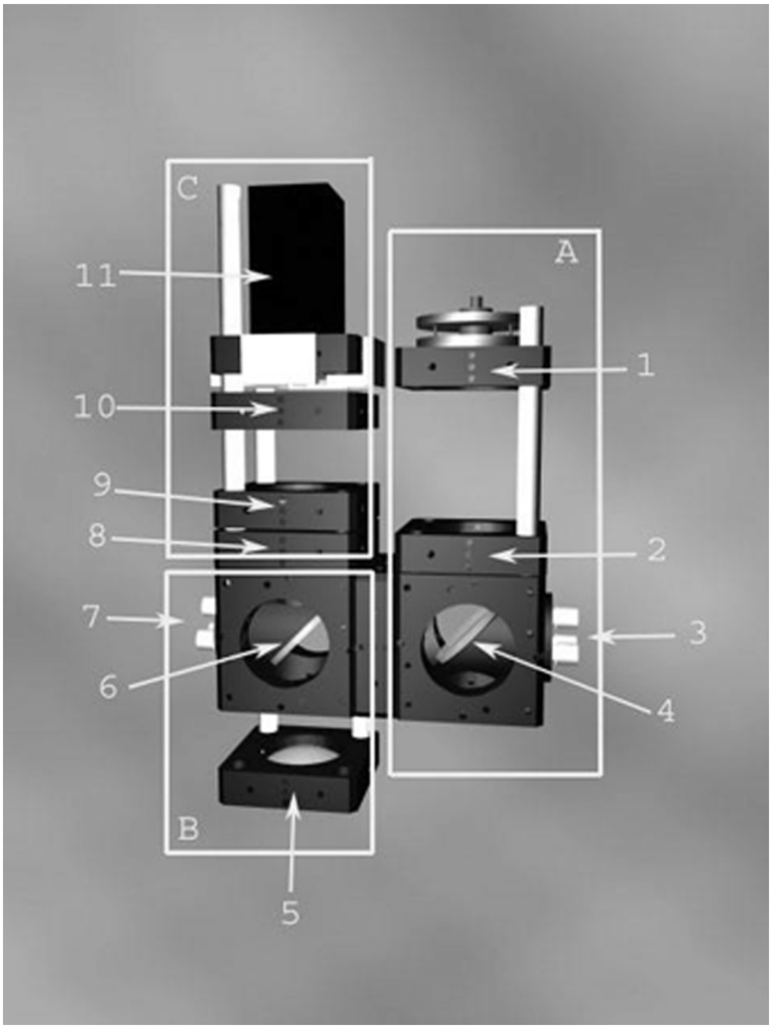

Fig. 2. Schematic of the assembled confocal optics. Subsystems A, B and C may be disconnected from the optics, thus easing alignment and focusing (Materials and Methods). Specific items include: (1) fiber optic coupling (Oz optical SPH-01 & HUCO-13); (2) 50-mm focal length achromatic lens (Spindler & Hoyer 06-3125); (3) beam steering adjustments (Spindler & Hoyer 06-5086); (4) silver elliptical plane mirror (Spindler & Hoyer 34-0523); (5) 50-mm focal length achromatic lens (Spindler & Hoyer 06-3125); (6) dichroic beam splitter (Spindler & Hoyer BSP-25-488514); (7) beam steering adjustments (Spindler & Hoyer 06-5086); (8) 40-mm focal length achromatic lens (Spindler & Hoyer 06-3127); (9) long wave pass filter 495 nm cutoff (Spindler & Hoyer LWP-25-490); (10) pinhole spatial filter, 0.6 mm (Spindler & Hoyer 04-0177); (11) PMT (Hamamatsu H5783).

sition is synchronized to the rotor using the leading edge of the rotor timing pulse, obtained as a TTL-compatible signal from the XLI data acquisition board. The leading edge of the rotor timing pulse clocks a divide-by-two circuit whose output is a square wave having a period equal to one revolution of the rotor. When the A/D is enabled, the square wave provides the gating signal for data acquisition. Digitized intensities are acquired directly into the data storage module. A pretriggering circuit enables storage of data digitized for a period preceding the edge of the gating signal, thus ensuring that data are obtained from a complete rotation. The data acquisition software permits intensity data from several consecutive turns of the rotor to be accumulated in the memory module, which enhances signal averaging. The clock rate of the A/D is adjusted by the data acquisition software to ensure that the intensities accumulated from all of the revolutions will fit in the data storage module.

After acquisition, data in the storage module may be transferred to the computer memory for manipulation as an integer array. The index of the integer array corresponds to angular positions around the rotor, with zero degrees nominally being the edge of the rotor timing pulse. In fact, as has been described previously, the propagation delay of the rotor timing pulse leads to a speed-dependent shift in the apparent position of the rotor timing pulse [2] that must be accounted for when calculating angular positions. Compensation for the propagation delay is accomplished in this system by decreasing any index by an amount corresponding to the number of A/D clock pulses equal to the propagation delay.

The intensity data for any given cell sector corresponds to a range of indices in the array of intensities. To calculate the starting index for a cell sector, the number of A/D clock pulses per revolution is multiplied by the fractional angular position of the cell (i.e. the cell angle divided by 2π). The index of the last intensity for the cell sector is calculated in the same way, using fractional angular position of the cell plus the width of the cell sector. In practice, the data acquisition software allows the experimenter to select the starting and ending angles of the cell sector. These sector angles are saved by the program and need to be determined only once for a given type of centerpiece and rotor type. The number of intensities acquired across a two-degree cell sector varies from two or three at 60 000 rpm to several dozen at lower rotor speeds. The intensities across a cell sector are accumulated for averaging.

For rotor data acquired over several rotations, an offset corresponding to the number of clock pulses per revolution, adjusted for the pre-trigger and propagation delay times, is calculated. By adding this offset to the indices for any cell sector, new indices are calculated for the intensities of that sector during the subsequent revolution, thus allowing the intensities for that revolution to be accessed. Adding the same offset to these new indices provides the intensity data for the next revolution of the rotor, and so on. This procedure provides a very rapid and efficient means to accumulate the intensity data for a cell sector. The intensity reported at each radial position is the average of the intensities accumulated over all of the rotations, and range from a dozen to hundreds of individual intensity measurements.

The data acquisition software collects fluorescence intensity data at user-specified intervals, saving the data for each sector in a separate file. The format of the data in the file corresponds to that used by Beckman for radial absorbance scans: two header lines that contain a user-supplied comment and the machine information (time, temperature, etc.) needed to analyze the data, followed by three columns of data containing the radial position, the average intensity and the standard deviation of the average intensity. The file format may be read by most of the existing sedimentation data analysis programs.

3. Optical alignment and focusing

Alignment and focusing of the fluorescence detector is accomplished in four stages. Caution should be exercised to avoid direct exposure of the eyes to the laser beam.

3.1. Stage 1

With Section A (Fig. 2) detached, the position of the first lens (Fig. 2(2)) is adjusted until the beam is collimated. Collimation is confirmed by comparing the diameter of the beam immediately exiting the optics to the beam diameter several meters away.

The optics is installed in the open vacuum chamber with sections A and B (Fig. 2) reconnected, but Section C detached. A disk cut from a white index card is placed on top of a centerpiece in a cell lacking the top window and window holder. The cell is inserted into a rotor and the rotor positioned so that the card is directly below the optics. With this configuration the objective lens (Fig. 2(5)) is adjusted until the spot size at the card is minimized.

Section C (Fig. 2) minus the PMT (Fig. 2(11)) is reconnected to the optics and the cell with the cutout index card is replaced with a cell (any type of centerpiece will do) containing a brightly fluorescing sample (e.g. >5 mM fluorescein) so that the fluorescence signal may be observed easily by eye when the cell is positioned in the excitation beam. This configuration is used to adjust the final achromatic lens (Fig. 2(8)) to maximize the light passing through the pinhole spatial filter (Fig. 2(10)). With the pinhole removed from the optics and in dim room light, a quick estimate of the focal point of the final lens is made using a white index card. Then the pinhole spatial filter (Fig. 2(10)) is substituted for the index card and positioned until the spot size on the face of the pinhole is minimized. Viewing the illuminated face of the pinhole may be accomplished using a small, hand-held mirror. At this point, the beam is focused on the plane of the pinhole, but the position of the focused spot needs to be centered on the pinhole. To center the spot, the beam steering mirror (Fig. 2(4)) is adjusted until light from the sample may be seen through the pinhole (Fig. 2(10)). The dichroic mirror angle (Fig. 2(6)) is adjusted for maximum emission intensity. Both adjustments are repeated until the intensity no longer improves and the focal position remains correct, as judged by the symmetry and intensity of the spot. At this point, the optics have been aligned and focused grossly. The following steps are necessary to optimize the focus.

3.2. Stage 2

In order to optimize the focus and alignment, the PMT is replaced with a graduated reticule. On top of this reticule, a second magnified, reticule is placed with its graduations perpendicular to the first reticule. A lens holder is slipped as a collar over the magnified reticule to hold it in place. The fluorescent sample is replaced by a cell that has a mirrored window in place of the top window, with the mirrored surface on the centerpiece side of the window. This arrangement roughly approximates a sample–window interface. The wavelength filter (Fig. 2(9)) in Section C is removed to allow some of the reflected light to be visible from above. With the laser attached and running, the chamber open, and the rotor halted, the lens positions in sections B and C are adjusted to maximize spot intensity on the reticule. Following this step, the reticules are removed and replaced by the pinhole, and the bright-fluorescent sample is positioned under the beam.

3.3. Stage 3

Because the aluminum heat sink of the XLI warps when vacuum is applied, the third and fourth stages of alignment and focusing must be done under vacuum. In order to observe the effects of alignment, the steel door on the XLI is replaced with a 1/2-inch thick aluminum plate containing a 1/2-inch thick by 6-inch diameter Lexan window located above the optics so that the fluorescence emission can be observed through the pinhole. With the laser attached and running, and the rotor stationary, the drift of the spot position is observed while the machine is coming to vacuum. The vacuum is broken and the alignment is adjusted by changing the dichroic mirror position (Fig. 2(7)) and the focus is adjusted by moving the lenses (Fig. 2(5 and 8)) to counteract the drift. These steps are repeated until the light intensity at the pinhole is maximized under vacuum. It should be noted that after this step, the optics will no longer be focused in open air.

3.4. Stage 4

Again, the chamber door is replaced by the Lexan window and the PMT is removed so that fluorescent light coming through the pinhole may be observed by eye. The rotor is balanced so that the brightly fluorescent sample may be spun. The machine is brought to vacuum at 20 °C, and the rotor is spun at 3000 rpm. While the rotor is coming to speed, the light from the pinhole is observed and any loss of signal intensity is noted. The machine is stopped and the dichroic mirror adjusted (Fig. 2(7)) to counteract these changes.

These steps are repeated until the intensity is maximized. No change in the intensity was observed when the rotor speed was raised to 6000 rpm. Observations made later using the PMT detector indicate that there is no further speed-dependent drift in the focus and alignment. The centrifuge is then reassembled, and the wavelength filter and the PMT reattached.

4. Methods

4.1. Materials

Bovine serum albumin (BSA), Cohn fraction V, was purchased from Sigma, No. A-2153, Lot 123F-6291, and dissolved in 50 mM Tris–HCl, pH 8.5. Ovalbumin, Grade III, was purchased from Sigma, No A-5378, Lot 58H700A. Fluorescein reference standard was purchased from Molecular Probes, F-1300, Lot 3561-1. Purified green fluorescent protein (GFP) was a gift from Dr G. Eric Schaller (University of New Hampshire) and was pure as judged by SDS PAGE.

4.2. Calibration of the radial position

The radial position (r, in cm) is calculated as

$$r = 5.850 + [0.0002(N - C)]$$

where N is the number of 2-μm steps the stepping motor has moved from its home position and C is the number of steps from the home position needed to center the excitation beam at the radial calibration point of 5.850 cm. This calibration position corresponds to that used for the XLI absorbance optics, and is defined by aluminum alignment fins that protrude into the inner radial holes of the counterweight. A modified counterweight is used for calibrating the fluorescence system. After carefully noting its orientation, the inner alignment fin is removed from a counterweight and a 1-mm deep by 1-mm wide groove is milled the length of its topside edge. The groove allows for a thin stripe of P-1000 phosphorescent paint to be applied. After the paint is dried, the fin is replaced in the counterweight, paint side up. When the counterweight was installed in an AN-Ti60 rotor, the distance from the center of the rotor to the edge of the fin was measured using a comparator and found to be 5.850 ± 0.002 cm. The modified counterweight still may be used for calibrating all of the optical systems.

To calibrate the radial positioning system of the fluorescence optics, the counterweight is balanced in the rotor and the centrifuge brought to vacuum and temperature at 3000 rpm. A radial scan of the counterweight is taken, and the midpoint of the fluorescence intensity change from the painted fin to vacuum defines the radial calibration position. The number of steps from home of the radial positioner is stored as the calibration point, C. The radial calibration needs to be redetermined only if the optics is readjusted or the centrifuge drive is changed.

4.3. Sensitivity

In order to assess the lowest concentration detectable by the fluorescence detector, a 2:1 dilution series of fluorescein [$\varepsilon_{488} = 8.8 \times 10^4$/cm M] in 20 mM Tris–HCl pH 8.1, 150 mM NaCl, 2.5 mM $CaCl_2$ was made using a starting concentration of 24 mM. Experiments were performed in six-channel charcoal-epon equilibrium centerpieces and quartz windows. With the machine running at 30 000 rpm and 20 °C, scans of the fluorescence intensity were acquired at a radial step size of 20 μm. At each radial position, average intensities were calculated from data acquired during 5 revolutions of the rotor. The A/D input voltage range and PMT voltage were adjusted for optimum signal-to-noise ratio for each fluorescein concentration. The laser intensity was held at 50% full power for concentrations above 1.0×10^{-6} M, and was held at 100% for lower concentrations.

4.4. Linearity

In order to provide useful data, the fluorescence detection system must exhibit a linear response with regard to fluorophore concentration. The experimental conditions used to test linearity were the same as those for assessing the sensitivity, except that the PMT voltage and laser power were held constant for each decade range in concentration. For all measurements, the A/D input voltage range was held constant at 0–5 V. The PMT voltage and the laser power were adjusted to optimize the signal intensity for any given decade range of concentrations. Linearity was tested by fitting a straight line to the plot of the fluorescence intensity vs. fluorescein concentration, using ORIGIN (Version 6.0, OriginLab Corp., Northampton, MA).

4.5. Radial resolution

The first derivative of a scan across a sharp fluorescence boundary produces a peak whose half-width at half-height is an estimate of the radial resolution. To determine the radial resolution in this manner, any scan with an abrupt fluorescence intensity change can be used. For the measurement reported here, the transition from the sample to the base of the channel of a six-channel equilibrium centerpiece was used. The derivative of the fluorescence intensity was taken using ORIGIN, with no smoothing applied to the data.

4.6. Comparison of the performance of the fluorescence and the absorbance optical systems

Sedimentation equilibrium and sedimentation velocity data were acquired for GFP using either the absorbance or fluorescence optical systems. These data allow for the comparison of the noise characteristics for the two optical systems, and permit an assessment of the accuracy of the molecular weight, sedimentation coefficient and diffusion coefficient obtained from analysis of fluorescence data.

4.6.1. Equilibrium

GFP at 11.4 μM was dialyzed against 20 mM Tris–HCl pH 8.1, 150 mM NaCl, 2.5 mM $CaCl_2$. Absorbance data were acquired using an unmodified XLI at a radial spacing of 20 μm for samples at 1:1, 1:3 and 1:9 dilutions in a six-channel, charcoal-epon centerpiece spun at 30 000 rpm and at 20 °C. The absorbance data were compared with fluorescence data acquired for 1:1, 1:3 and 1:9 dilutions of a 435 nM stock GFP solution run at 30 000 rpm and 18 °C. Data were acquired at a radial spacing of 20 μm, averaging intensities for 5 rotor revolutions at each radial position. For the fluorescence data, the laser intensity was set to 50% with the A/D input voltage range set to 0–5 V and the PMT voltage at 60%. Data were analyzed using NONLIN, fitting the data to a model of a single ideal species [3]. Molecular weights were calculated with SEDNTERP using a calculated partial specific value of 0.730 ml/g, and a calculated solvent density of 1.0074 g/ml.

When using six-channel equilibrium centerpieces, the bottom of the channels farthest from the center of rotation were partially obscured by the cell assembly screw. Fluorescence data from the obscured region were excluded from analysis.

4.6.2. Velocity

For the absorbance detection, 9.05 μM GFP was dialyzed against 20 mM Tris pH 8.1, 150 mM NaCl, 2.5 mM $CaCl_2$ and run at 30 000 rpm and 20 °C. Absorbance data were acquired using 'continuous mode' detection at a nominal radial spacing of 30 μm. These absorbance data were compared with fluorescence data acquired using 90.5 nM GFP dialyzed against the same solvent and run at 40 000 rpm, 18 °C, with data acquired at a radial interval of 20 μm, averaging intensities from 5 rotor revolutions at each radial position. The laser intensity was set to its minimum with the A/D input voltage range set to 0–5 V and the PMT voltage at 50%. Data were analyzed using SEDFIT, kindly modified by Dr Peter Schuck to accommodate fluorescence intensity data [4].

4.7. Fluorescence detection in the presence of nonfluorescent protein

One of the advantages of fluorescence detection is its ability to discriminate fluorescently labeled protein from unlabeled protein. Accordingly, sedimentation velocity and sedimentation equilibrium experiments were conducted in which trace quantities of GFP were monitored in solutions containing nonfluorescent protein.

4.7.1. Velocity

GFP at 9.0 μM was analyzed in a charcoal-filled double-sector centerpiece in a solution that also contained 40 mg/ml BSA, 50 mM Tris–HCl, pH 8.5, at 30 000 rpm and 18 °C. Data were collected at a radial interval of 20 μm, averaging five intensities at each radial position. The laser intensity was set to 75% of full power, the A/D input voltage range was set to 0–5 V and the PMT voltage was set at 75%. The midpoint of the fluorescence intensity boundary, R, was determined manually from graphs of the raw data, and the apparent sedimentation coefficient was determined from the slope of the graph of $\ln R$ vs. $\omega^2 t$.

4.7.2. Equilibrium

GFP at 2.0 μM in solutions of 150 mM NaCl, 50 mM Tris, pH 8.5 and containing varying background concentrations of ovalbumin was analyzed at 20 000, 30 000 and 40 000 rpm, at 18 °C. Data were collected at 20-μm intervals, averaging the data from 2 revolutions of the rotor at each radial position. The laser intensity was set to 50% full power with the A/D input voltage range set to 0–5 V, and the PMT voltage set at 70%. The background concentrations of ovalbumin used were 50, 20, 10, 5 and 1 mg/ml. Fluorescence intensity data were analyzed using WinNONLIN (available from the RASMB download site at the Boston Biomedical Research Institute, www.bbri.org). No single model fit all of the data adequately which, given the complexity of the system, was not surprising. Accordingly, reduced molecular weights were determined using the model of a single ideal component. For data acquired using the absorbance or interference optical system, this reduced molecular weight usually falls between the weight- and z-averages. However, fluorescence data from a system containing high concentrations of nonfluorescent material should not be considered to provide any defined molecular weight unless it is clear that the quantum yield of the fluorescent component is constant over all experimental conditions. In the absence of experimental values of the quantum yield, we report the molecular weights as apparent values without reference to specific averages. In order to calculate the apparent molecular weights, buffer densities were estimated from tabulated values for proteins at high concentrations. The apparent partial specific volume for GFP was assumed to be invariant in the presence of high concentration of ovalbumin, much as has been observed for BSA at high concentrations [5]. It should be noted that this assumption may not hold in general, and should be the subject of further studies.

A 60 mg/ml stock solution of ovalbumin was dialyzed against 150 mM NaCl, 50 mM Tris, pH 8.5, and was examined alone by sedimentation equilibrium, using interference optics, in a six-channel equilibrium cell. Data were collected for the stock solution, and 17 serial 2:1 dilutions of this stock solution at 20 °C and at 20 000, 30 000 and 40 000 rpm.

5. Results

5.1. Sensitivity

One of the potential benefits of using a fluorescence detection system is an increase in sensitivity, which was assessed using serial dilution of fluorescein (Fig. 3). Under the conditions of these experiments, fluorescein is nearly neutrally buoyant, so the average intensity from each channel, calculated from the central two-thirds of the radial scan, provides a single data point for each dilution. The minimum detectable concentration in these experiments was ~288 pM (Panel D). The slope of the data provides another assessment of the detector's sensitivity, with a larger slope indicating a higher sensitivity and, therefore, a lower minimum detectable concentration. The concentration that corresponds to zero signal for each of the panels is considered the apparent minimum detectable concentration. Comparison of the slopes of the lines in Fig. 3 shows that there is a systematic decrease in detector sensitivity at higher concentrations of fluorophore, resulting in a systematic decrease in the apparent minimum detectable concentration from ~70 nM (Panel A) to 0.09 nM

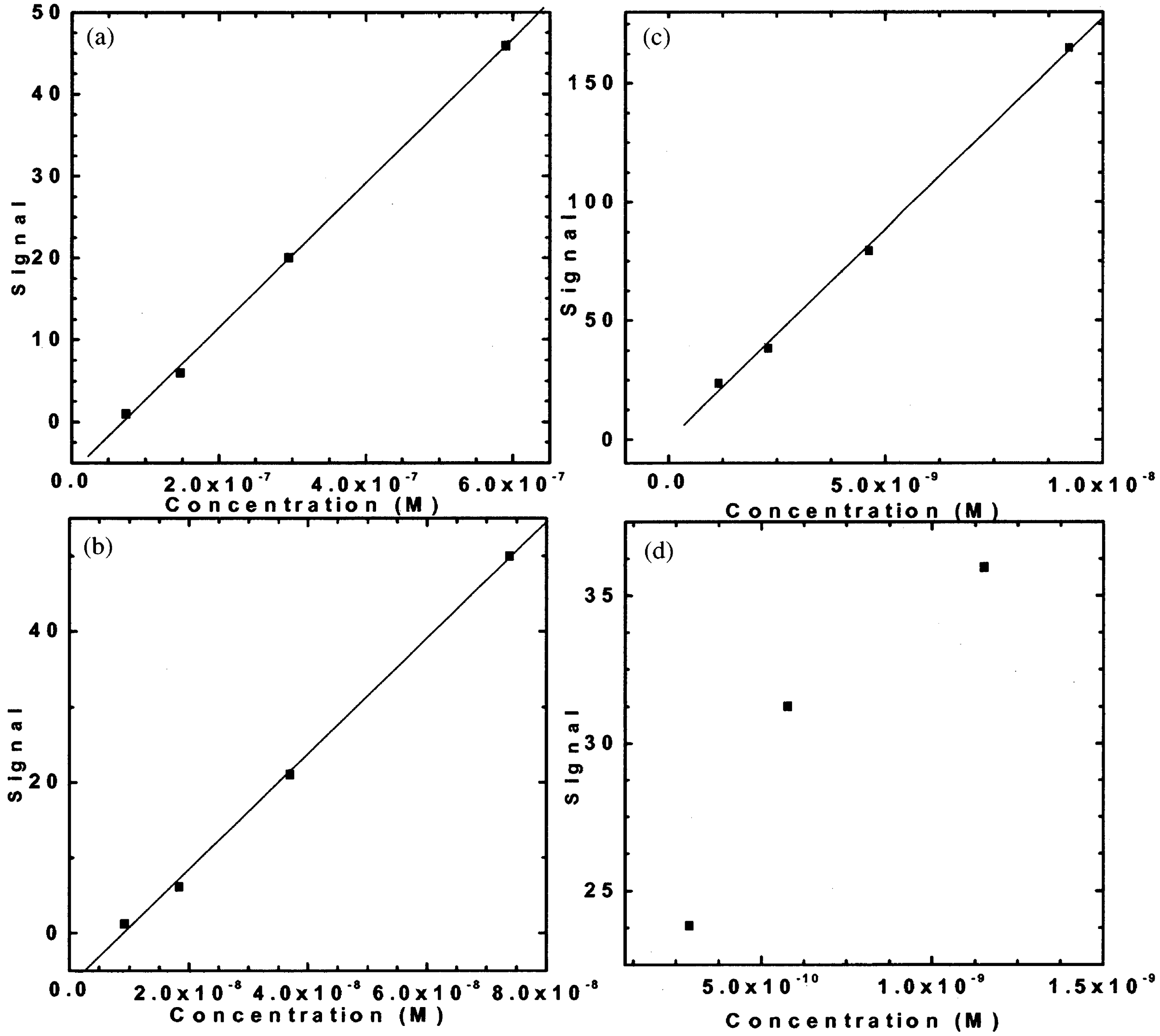

Fig. 3. Sensitivity and linearity. Relative fluorescence intensity vs. concentration for a serial dilution of fluorescein (Materials and Methods), along with the best fit straight line. The laser intensity and PMT voltage were adjusted for each set of concentrations to optimize signal clarity. Each panel displays data from approximately a one-decade concentration range of fluorescein. Panel A: 73.7–590 nM, with a slope of $8.7\pm0.4\times10^7$/M and an intercept of -5.9 ± 1.4, $R=0.9978$, yielding an apparent minimum detectable concentration of 69.9 nM. Panel B: 9.2–73.7 nM, with a slope of $7.5\pm0.3\times10^8$/M and an intercept of -6.2 ± 1.3, $R=0.9983$, yielding an apparent minimum detectable concentration of 8.96 nM. Panel C: 1.15–9.22 nM, with a slope of $1.74\pm0.1\times10^{10}$/M and an intercept of -0.24 ± 5.0, $R=0.9972$, yielding an apparent minimum detectable concentration of 0.09 nM. Panel D: 0.288–1.15 nM was not fit to a straight line due to the pronounced downward curvature of the data. However, these data show that the system is capable of detecting fluorescein at a concentration ~300 pM.

(Panel C) as the range of concentrations examined becomes more dilute. This systematic shift is most likely a consequence of the inner-filter effect (below).

Using an extinction coefficient of 8.8×10^4/cm M for fluorescein at 490 nm with the quantum yield at this wavelength of 0.97, the detection limit of other fluorophores can be estimated as

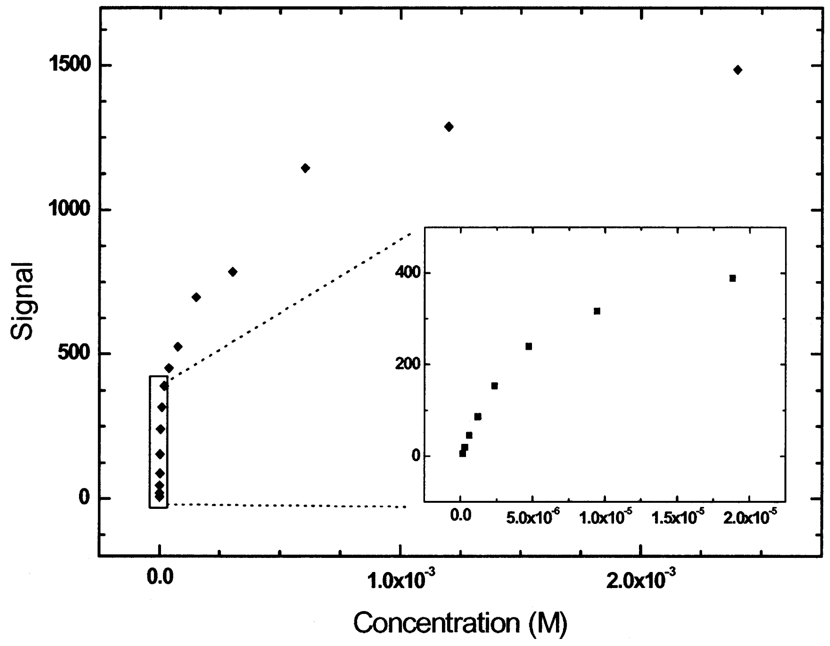

Fig. 4. Fluorescence intensity as a function of the cell loading concentration for fluorescein over a wide concentration range. The data exhibit curvature typical of what is observed with the inner filter effect. Laser intensity was set to 50% with a PMT voltage of 60%. Scans were taken with 20-μm steps averaging 5 intensities per step.

$$C\ \mathrm{min} = 2.88 \times 10^{-10}\ \mathrm{M}\ \frac{(8.8 \times 10^{4}/\mathrm{cm\ M})(0.97)}{(\varepsilon_{\mathrm{M}})(Q)} \tag{1}$$

where ε_{M} is the molar extinction coefficient of the fluorophore of interest and Q is its quantum yield.

5.2. Linearity

In order for the fluorescence intensity to be used as a measure of concentration without correction using external standards, the intensity must be directly proportional to the fluorophore concentration. While it is desirable for the linearity of signal to concentration to apply over as wide a concentration range as possible, sedimentation analysis of individual samples typically requires linearity to span a one-decade range in concentration. To assess the linearity of the fluorescent intensity with concentration, data from the serial dilution of fluorescein were separated into one-log ranges (Fig. 3).

Panels A, B and C show the relative fluorescence intensity observed as a function of fluorescein concentration over one-log concentration ranges between 1 and 600 nM. Each of these panels shows the data fit to a straight line, with only minor deviations, indicating that a reasonable linear correspondence may be expected for individual experiments having loading concentrations in this range. Linearity was not tested above 600 nM, where data from the absorbance system will most likely be available.

At the lowest concentration range (Panel D), the fluorescence intensity exhibits a significant downward curvature. While the cause of this curvature is not entirely certain, the data are consistent with tight, saturable binding of fluorescent material to the cell walls. Binding of this sort will result in a constant amount of dye being lost to the walls, which corresponds to a greater fractional amount of dye being lost at low loading concentrations

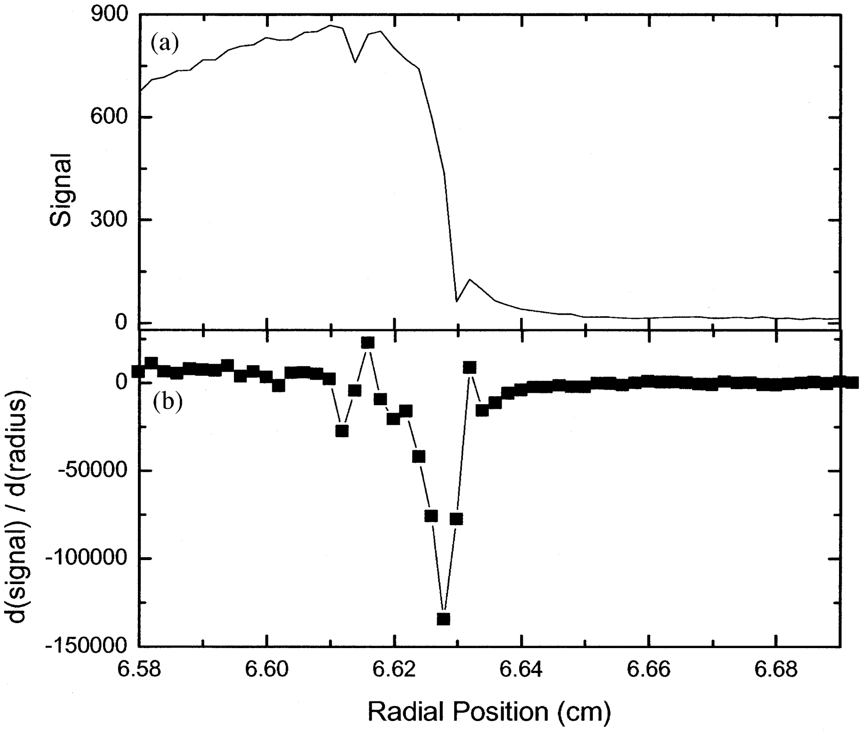

Fig. 5. Estimate of the radial resolution. GFP at 2.0×10^{-6} M in 100 mM Tris–HCl pH 8.5. Sample was spun at 30 000 rpm at 20 °C in a six-channel equilibrium cell. Laser intensity was set to 50% with a gain of 5 V unipolar and a PMT voltage of 70%. Scans were taken with 20-μm steps averaging 2 scans per step. The sample has already come to equilibrium. Panel A shows the base of channel B of a six-hole equilibrium centerpiece. Panel B shows the first derivative of panel A.

than at higher loading concentrations. The result is a roll-off of the intensity at low dye concentrations. The presence and extent of binding to the walls will depend both on the dye and cell wall material (including the cleanliness of the cell wall). Thus, the linearity of the signal will involve characteristics of the sample as well as characteristics of the apparatus, particularly at low dye concentrations.

Over a much broader concentration range (Fig. 4), the signal roll-off typical of the inner-filter effect is visible. This roll-off will lead to underestimates of the molecular weight and overestimates of the second virial coefficient from sedimentation equilibrium data. The analysis of sedimentation velocity data affected by the inner-filter effect will tend to provide an underestimate of *s* and an inability to fit the boundary shape well (i.e. estimates of *D* will be inaccurate). While it is not possible to predict the magnitude of these effects a priori, these effects will be most pronounced at high concentrations (>0.5 μM for a fluorophore like fluorescein), or for data that span a broad concentration range. At the concentrations of fluorophore likely to be used in the centrifuge, the roll-off should not interfere with data analysis.

5.3. Radial resolution

A high radial resolution is needed to measure the concentration distribution accurately. Experience with absorbance optics has shown that radial resolutions of 20 μm or so are adequate for most purposes, even though a higher resolution is desirable. An estimate of the radial resolution may be obtained from the intensity data at a sharp boundary. Fluorescence intensity profiles at the base of a centerpiece, where the signal drops from a finite value to zero, will produce results similar to those shown in Fig. 5. Panel A shows the signal decrease from a 2.0×10^{-6} M GFP sample to the septum of a non-fluorescing centerpiece, and Panel B shows the first derivative of these data. At half-height, the derivative yields a half-width of 1–2 data points, corresponding to 20–40 μm. This is a typical result, confirmed using a variety of dyes, rotor speeds and data acquisition parameters (data not shown), and we conclude that the radial resolution for these optics is approximately 30 μm.

5.4. Comparison of data from absorbance and fluorescence optics

5.4.1. Sedimentation equilibrium

Equilibrium sedimentation data for GFP acquired using the absorbance optics (Fig. 6A) or the fluorescence optics (Fig. 6B) fit adequately to a model consisting of a single, ideal thermodynamic component. The molecular weight determined from the absorbance data varies from sequence molecular weight (26.9 kDa) by less than 1%, whereas the molecular weight determined from the fluorescence optics differs from the sequence molecular weight by approximately 3%. These results confirm that it is possible to determine accurate molecular weights from sedimentation equilibrium data using the fluorescence detector. The generality of this observation, though, is dependent on the linearity of the fluorescence signal with concentration, which can be dependent on the peculiarities of the chemical system (Section 6).

The residuals from a curve fit to the data can provide insights into the nature of the noise in signals. For the absorbance system, the noise characteristically is stochastic, with a high spatial frequency (Fig. 6A, inset). For the fluorescence system (Fig. 6B, inset), the noise is largely random, though there is evidence of a systemic intensity drift (i.e. ‘wavy’ noise of low spatial frequency). The drift is reproducible from scan to scan (e.g. the velocity data in Fig. 7), but not from cell to cell or experiment to experiment. Tests comparing sapphire and fused-silica windows produce similar variations (not shown), suggesting that window polarization effects are unlikely to be the cause. Although drifts in the signal of this magnitude are observed frequently, their origin is unknown.

For the data in Fig. 6, the root-mean-square error of the noise for the absorbance system is 5.93×10^{-3}, obtained over a signal spanning 1.32 absorbance units, yielding an estimated signal-to-noise ratio of 223. For the fluorescence system, the equivalent values are a root-mean-square error of the noise of 5.22×10^{-1} for a signal spanning 33.5 units, yielding an estimated signal-to-noise ratio of 64. This ~3.5-fold lower signal-to-noise ratio suggests that the precision of parameters obtained with the fluorescence detector will be somewhat less than those obtained from absorbance measurements, an expectation that is borne out in the molecular weight determinations for these data (above).

5.4.2. Sedimentation velocity

A comparison of parameters for sedimentation velocity data acquired using the absorbance system (Fig. 7) and the fluorescence system (Fig. 8) are presented in Table 1. For both optical systems, the data could be fit adequately as a single ideal hydrodynamic component. The lower values of s and D obtained from the fluorescence data are a consequence of the lower experimental temperature. (Damage to the radiometer during modifications to the XLI caused the instrument read 20 °C, even though subsequent measurements revealed that the radiometer calibration was off.) Note, however, that the molecular weights calculated from both systems are consistent with one another and are within reasonable error of the true molecular weight. The molecular weight obtained from fluorescence data varies from the absorbance data by less than 1% and both differ from the expected value by less than 1%.

Panel C in both Figs. 7 and 8 presents the residuals as a grayscale bitmap. These bitmaps ordinarily are used to assess the quality of the fit to the data. A proper fit will produce a uniform, neutral-gray bitmap, such as is seen for the absorbance data (Fig. 7C). A poor fit to the data will produce characteristic diagonal stripes of lighter and darker gray.

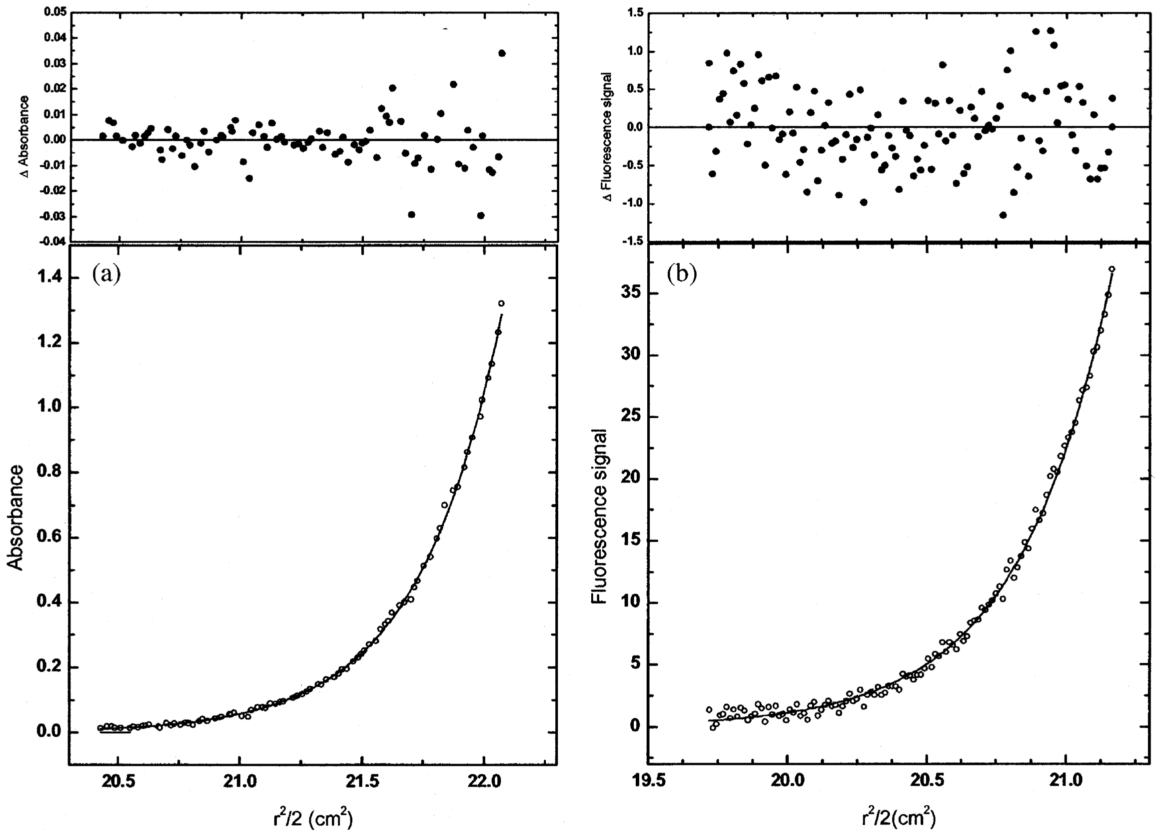

Fig. 6. Comparison of equilibrium sedimentation data. GFP in 20 mM Tris–HCl pH 8.1, 150 mM NaCl, 2.5 mM $CaCl_2$ at 20 °C and 30 000 rpm. Panel A: Absorbance data acquired after equilibrium has been reached for 1.14×10^{-5} M GFP. Non-linear least squares curve fitting yields $\sigma=2.905\pm0.130$, corresponding to a molecular weight of 27.0 ± 1.2 kDa. Panel B: Fluorescence data acquired after equilibrium has been reached for 4.35×10^{-7} M GFP. Non-linear least squares curve fitting yields $\sigma=2.984\pm0.240$, corresponding to a molecular weight of 27.7 ± 2.2 kDa.

Because the absorbance data (Fig. 7C) show that GFP can be fit well as a single, ideal hydrodynamic monomer, it is expected that the bitmap for the fluorescence data (Fig. 8C) also should be a uniform neutral-gray, which it is not. The systematic errors revealed in this bitmap provide insights into the nature of the noise on the fluorescence signal. Rather than diagonal stripes in the bitmap, indicating a poor fit to the model, single horizontal lines show deviations from the normal. Furthermore, within a stripe, there are regions where the grayscale is bright, with compensating regions where the grayscale is darker. This pattern strongly suggests that the fluorescence intensity was offset for some portion of the scan, but not offset in the other portions of the scan. The causes and correction of these fluctuations are being investigated as an improved system is developed.

5.5. GFP in the presence of non-fluorescent protein

The vast majority of biological reactions occur naturally in an environment that is far from ideal because of high concentrations of surrounding macromolecules. The nonideality is manifested in both the thermodynamics and hydrodynamics of the molecules. In order to understand the behavior of molecules in concentrated solutions, it is nec-

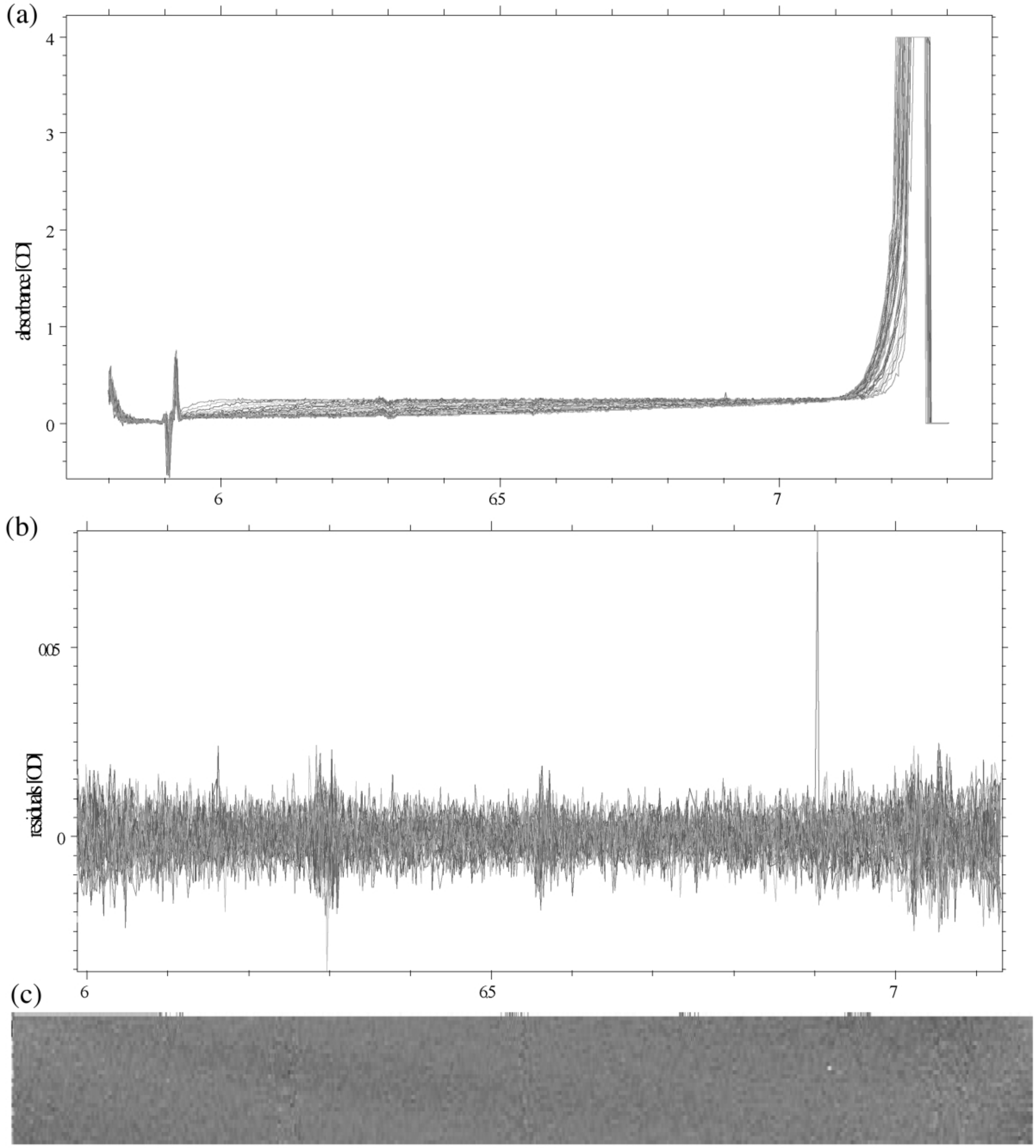

Fig. 7. Sedimentation velocity analysis of GFP using absorbance optics. SEDFIT analysis of absorbance for 9.05×10^{-6} M GFP in 20 mM Tris–HCl pH 8.1, 150 mM NaCl, 2.5 mM $CaCl_2$, run at 30 000 rpm, at 20 °C. Meniscus position was fixed at 5.9339 cm, cell bottom was fixed at 7.2246 cm. *M*, *s*, the baseline, time-invariant noise, and radial-invariant noise was floated during analysis. Panel A shows the raw data, panel B shows the residuals overlaid, and panel C shows the grayscale bitmap of the residuals. RMS for this fit was 0.005.

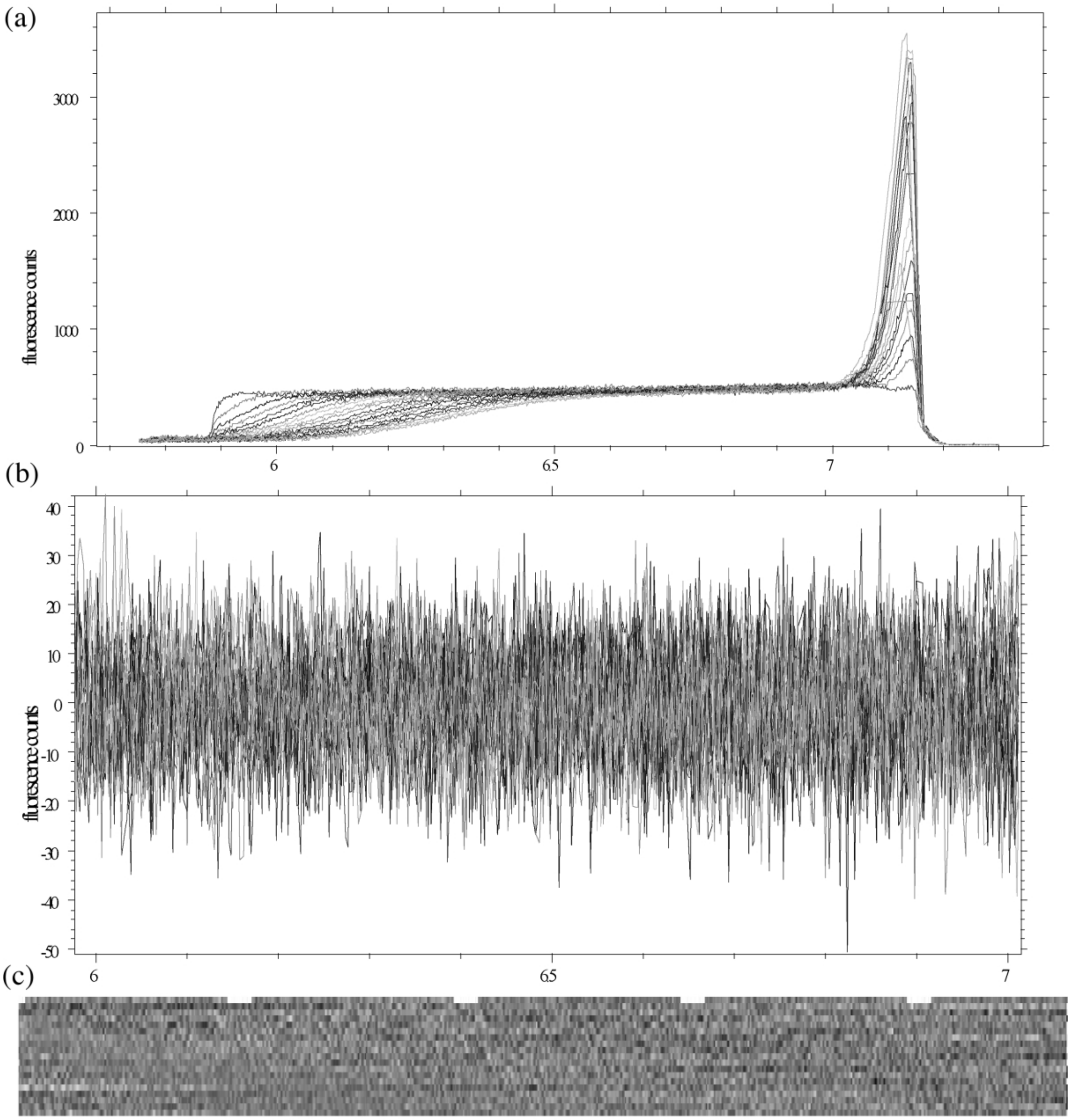

Fig. 8. Sedimentation velocity analysis of GFP using fluorescence optics. SEDFIT analysis of fluorescence data for 9.05×10^{-8} M GFP in 20 mM Tris–HCl pH 8.1, 150 mM NaCl, 2.5 mM $CaCl_2$, run at 40 000 rpm, at 20 °C. Meniscus position was fixed at 5.8868 cm, cell bottom was fixed at 7.1450 cm. *M*, *s*, the baseline, time-invariant noise, and radial-invariant noise was floated during analysis. Panel A shows the raw data, panel B shows the residuals overlaid and panel C shows the grayscale bitmap of the residuals. Each horizontal line is a scan whose grayscale is proportional to the deviations from the fit at each radial position. The vertical axis is the scan number, with the first scan at the top. RMS for this fit was 10.8.

Table 1
Comparison of sedimentation velocity results from the absorbance and the fluorescence optics

	T (°C)	s (S)	D (Ficks)	M (kDa)
Absorbance	20	2.70 ± 0.08	9.01 ± 0.315	27.1 ± 0.09
Fluorescence	18	2.50 ± 0.05	8.33 ± 0.353	27.0 ± 0.13

All values were obtained using SEDFIT. The meniscus and bottom were fixed during analysis. M, s, D and the baseline were fit during analysis. Also fit were the time-invariant and radial-invariant noise. The sequence molecular weight for the GFP is 26.0 kDa.

essary to have methods for assessing the behavior of relatively dilute concentrations of molecules in the presence of high concentrations of other macromolecules. Fluorescence provides one means of discriminating trace levels of molecules in spite of overwhelming concentrations of other, similar molecules.

5.5.1. Velocity

Results from an experiment in which 0.24 mg/ml GFP is sedimented in the presence of 40 mg/ml BSA are shown in Fig. 9. The fluorescence intensity data showing the GFP boundary is presented in panel A. Because these data do not exhibit a flat plateau concentration, we decided not to fit the data using a computer program. Instead, an estimate of the apparent sedimentation coefficient (2.03 ± 0.085 S) was determined as the slope of the best-fit line through a graph of the natural log of the position of the midpoint of the boundary vs. $\omega^2 t$ (Fig. 9B). This sedimentation coefficient is approximately 19% lower than that observed in the absence of BSA (2.50 S, Table 1).

A decrease in the sedimentation coefficient in the presence of a high concentration of protein is expected on hydrodynamic grounds, with the decrease observed here ($\Delta S/\Delta C$ of 0.0125/mg/ml) at the high end of what might be anticipated for globular proteins [6]. However, both GFP and BSA are anionic, and the Johnston–Ogston effect may be significant in this system [7]. Hydrodynamic nonideality also could be the cause of the sloped plateau (Fig. 9A), though further experiments would have to be done to characterize the effect. It is clear, however, that the fluorescence detector will be useful in future hydrodynamic studies.

5.5.2. Equilibrium

GFP at 2.06 μM was brought to sedimentation equilibrium in the presence of varying concentrations of ovalbumin. The profiles in Fig. 10 show that the fluorescence intensity is not affected by increasing ovalbumin concentrations. Hence, these data may be analyzed without concern for quenching effects. Fluorescence data were fit as described in Section 4 to provide estimates of the apparent molecular weight. In a separate sedimentation equilibrium experiment using interference detection, the apparent molecular weight of the ovalbumin was determined. Fig. 11 presents the effects of increasing ovalbumin concentration on the apparent molecular weight of both GFP and ovalbumin as the ratio of their respective apparent molecular weights to their sequence molecular weights. The values for molecular weight have been corrected for solution density changes due to the ovalbumin.

From the data in Fig. 11 it is evident that the apparent molecular weight of ovalbumin decreases roughly linearly with concentration. This linear decrease in apparent molecular weight corresponds to a nonlinear increase in its chemical activity, hence cannot be fit with a model that includes only a second virial coefficient. The GFP results shown in Fig. 11 present a steep decrease in $M_{\mathrm{app}}/M_{\mathrm{seq}}$ with relatively low concentrations of ovalbumin, followed by a leveling off of $M_{\mathrm{app}}/M_{\mathrm{seq}}$. These results suggest that with high background concentrations of ovalbumin there are compensating favorable interactions (either GFP–GFP or GFP–ovalbumin) that mitigate thermodynamic repulsive nonideality. Further experiments are planned to examine the root causes of this nonideality.

6. Discussion

Because of its sensitivity and selectivity, fluorescence detection will be a useful addition to the XLI analytical ultracentrifuge. Both the sensitivity and the radial resolution for the prototype system presented here are comparable to parameters

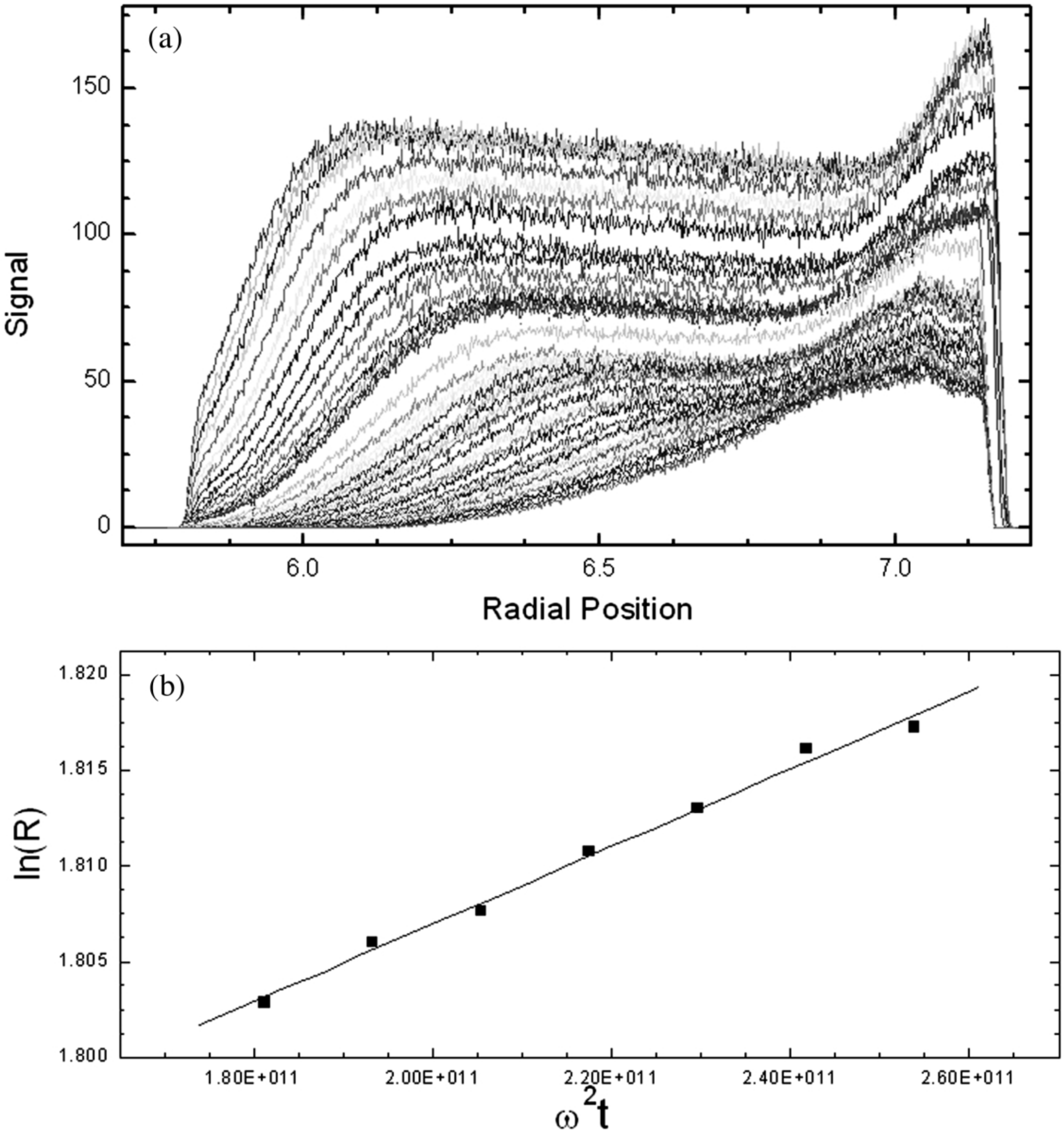

Fig. 9. Sedimentation velocity of GFP in the presence of high concentrations of BSA. Velocity sedimentation of a relatively low concentration (9.0×10^{-6} M, 0.243 mg/ml) of GFP in the presence of high concentrations (40 mg/ml) of a background molecule (BSA). Panel A shows the progression of scans as time passes. Panel B plots the boundary midpoint against w^2t from which the apparent sedimentation coefficient was determined.

obtained by Riesner for a system designed for the Model E [1]. Furthermore, the data presented here provides proof-of-concept for the front-face confocal design, which is more compact and amenable to mounting in the XLI. Although the precision of the concentration measurements are somewhat lower than with those obtained using absorbance optics, it is clear that estimates of s, D and M may be obtained with good accuracy from either equilibrium or velocity sedimentation experiments.

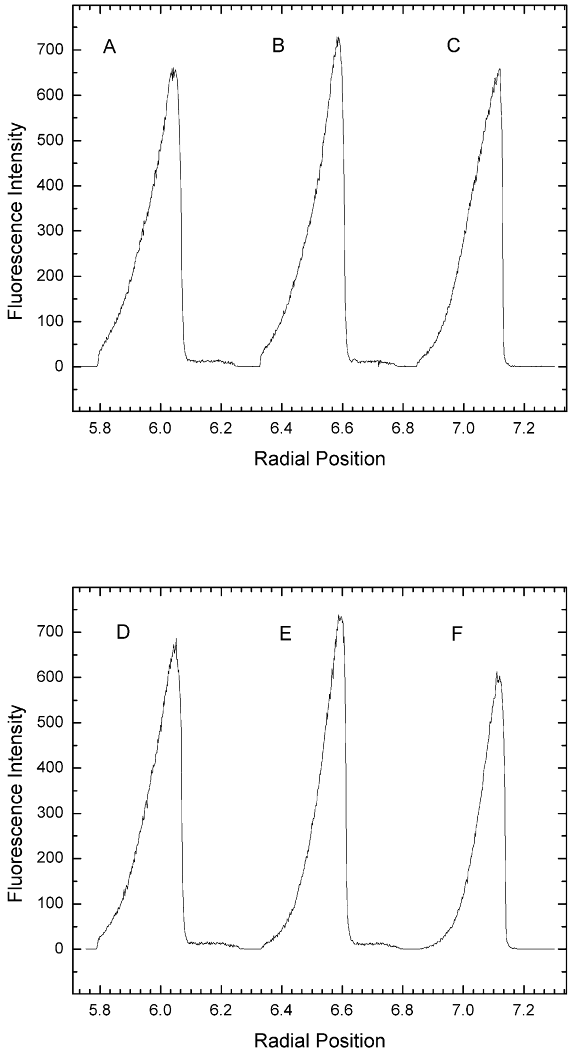

Fig. 10. Sedimentation equilibrium of GFP in varying concentrations of ovalbumin. A constant concentration of GFP (2.0 μM) brought to sedimentation equilibrium in the presence of varying concentrations of ovalbumin. Sample scans are shown to illustrate the signal strength. Channel A–F represent 50, 20, 10, 5, 1 and 0.5 mg/ml of background ovalbumin loading concentration, respectively. The loss of signal strength in the outer portion of channels C and F is due to the window screw ring of the cell obscuring a portion of the channel.

Useful data may be obtained for a fluorescein-like molecule at least over the range of concentrations from 1 to 600 nM. However, the linearity of the intensity with concentration appears to be limited to approximately one-log intervals over this range. For many ordinary uses, such as determining s, D or M for simple systems, this limitation will not be a serious impediment. However, for protocols that rely on obtaining data over a wider concentration range, or that require knowledge of absolute concentrations (e.g. determining equilibrium binding constants), the lack of linearity over a several-log concentration range would pose severe limitations. In these instances, it will be necessary to provide a set of reference standards that may be used to convert the measured intensity to concentration. In order to be useful, these standards must be run simultaneously with the samples, and the reference intensity data must be gathered using the same instrument settings (i.e. PMT voltage, A/D input gain) as the samples.

The detection hardware and software described here cannot overcome problems that are inherent to fluorescence intensity measurements. Therefore, problems such as that posed by the inner-filter effect (Fig. 4), while minimized in the present design, must be kept in mind when designing experiments. Likewise, any process or agent that alters the quantum yield of a fluorophore (e.g. quenching coupled with a reversible association) will affect both the precision and the accuracy of parameters extracted from the data. Again, careful experimental design and appropriate experimental controls must be employed to guard against these problems. It is important to note that these sorts of problems are inherent to the use of fluorescence intensity data as a measure of concentration and are not limitations of the apparatus presented here.

During 2 years of extensive testing, the design presented here proved to be quite reliable. Even so, there are three areas that will benefit from improvements to allow easy duplication and use. First, the Ar^+ laser poses several problems: it is expensive, it requires an expensive fiber and custom feedthrough to conduct the light into the vacuum chamber, it exhibits mid- and long-term intensity fluctuations that are difficult to allow for during data analysis (e.g. Fig. 8) and it routinely needs tedious and delicate alignment. Second, the stepping motor has required extensive routine maintenance to operate without failure in the vacuum. Finally, the data acquisition software

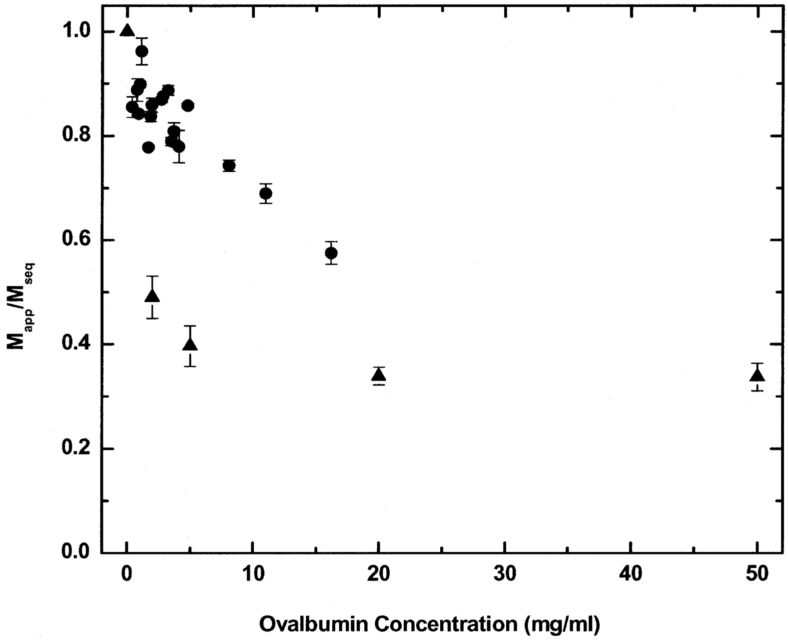

Fig. 11. Equilibrium sedimentation results for GFP in a high ovalbumin background. Data are presented as the ratio of the apparent molecular weight divided by the sequence molecular weight for GFP (▲) and for ovalbumin (●). At loading concentrations above 16 mg/ml, the concentration gradients for the ovalbumin were too steep to determine accurate estimates of the apparent molecular weight.

required specialized training, only worked under Windows 95/98 and used system resources so extensively that simultaneous operation of the absorbance and fluorescence system was not practical. Each of these limitations has been addressed, and a new fluorescence detection system is being tested that can be retrofitted readily to the existing XLI.

7. Conclusion

We anticipate that fluorescence-detected sedimentation analysis will be an extremely useful tool that brings the rigor of AUC to the study of interesting questions in biology and biochemistry. For example, it should be possible to obtain accurate size estimates of macromolecular complexes from crude sample preparations using labeled proteins (e.g. GFP constructs or using fluorescein-conjugated antibodies). Likewise, fluorescence-detected sedimentation should be an extremely valuable tool for the investigation of molecular interactions in crowded environments.

Acknowledgments

We are grateful to David Yphantis for his continued interest in the development of the analytical ultracentrifuge, even when such efforts were not fashionable. His enthusiasm, suggestions and encouragement always are appreciated. This work has been supported by NSF DBI-9876582 and the Center to Advance Molecular Interaction Science.

References

[1] B. Schmidt, W. Rappold, V. Rosenbaum, R. Fischer, D. Riesner, Colloid Polym. Sci. 268 (1990) 45–54.
[2] T.M. Laue, R.A. Domanik, D.A. Yphantis, Anal. Biochem. 131 (1983) 220–231.

[3] M.L. Johnson, J.J. Correia, D.A. Yphantis, H.R. Halvorson, Biophys. J. 36 (1981) 575–588.
[4] P. Schuck, Biophys. J. 75 (1998) 1503–1512.
[5] H. Durchschlag, Specific volumes of biological macromolecules and some other molecules of biological interest, in: H.-J. Hinz (Ed.), Thermodynamic Data for Biochemistry and Biotechnology, Springer, Berlin, Heidelberg, 1986, pp. 45–128.
[6] A.J. Rowe, Biopolymers 16 (1977) 2595–2611.
[7] J.P. Johnston, A.G. Ogston, Trans. Faraday Soc. 42 (1946) 789–799.